

In Situ Generated $\text{Yb}_2\text{Si}_2\text{O}_7$ Environmental Barrier Coatings for Protection of Ceramic Components in the Next Generation of Gas Turbines

Mateus Lenz Leite, Ulrich Degenhardt, Walter Krenkel, Stefan Schafföner, and Günter Motz*

In face of an accelerating climate change, the reduction and substitution of fossil fuels is crucial to decarbonize energy production. Gas turbines can operate with versatile fuel sources like natural gas and future fuels such as hydrogen and ammonia. Furthermore, thermal efficiencies above 60% can be achieved using non-oxide silicon-based ceramic components. However, water vapor is one of the main combustion products leading to rapid corrosion because of volatilization of the protective SiO_2 layer at 1200 °C. An in situ generated $\text{Yb}_2\text{Si}_2\text{O}_7$ double layered environmental barrier coating system composed of silazanes and the active fillers Yb_2O_3 and Si processed at 1415 °C for 5 h in air protects a Si_3N_4 substrate very effectively from corrosion. It exhibits a dense microstructure with a total thickness of 68 μm , overcomes 15 thermal cycling tests between 1200 and 20 °C and shows almost no mass loss after very harsh hot gas corrosion at 1200 °C for 200 h ($p_{\text{H}_2\text{O}} = 0.15 \text{ atm}$, $v = 100 \text{ m s}^{-1}$). The excellent adhesion strength ($36.9 \pm 6.2 \text{ MPa}$), hardness ($6.9 \pm 1.6 \text{ GPa}$) and scratch resistance (28 N) demonstrate that the coating system is very promising for application in the next generation of gas turbines.

CO_2 emissions should be cut in half by 2050 compared to 2009 in order to limit the increase in the world average temperature to 2 °C. Despite the advances in renewable energy alternatives, their supply strongly depends on favorable weather conditions and their efficient storage is still difficult. Thus, the key factor for the transition towards a more sustainable future relies on decarbonizing power generation. Along the substitution of heavy fossil fuels by natural gas can decrease the related emissions in $\approx 50\%$.^[1–4] Nevertheless, a developing interest has been shown for carbon-free sources as ammonia and liquid hydrogen, which are potential fuel alternatives to produce energy with a cleaner emission profile.^[5]

Besides the compactness and low maintenance costs, gas turbines can operate with versatile fuel sources, which make them a natural choice for the efficient production of energy.

For this reason, they have found increasing service in the past 40 years in the power industry both among utilities and industrial plants as well as for aviation.^[6] In combined cycle operation and with inlet temperatures exceeding 1400 °C, efficiencies as high as 63% can be achieved.^[2] Therefore, different strategies are adopted to protect the currently used Ni-based superalloys such as the deposition of yttria-stabilized-zirconia thermal barrier coatings (TBC) and intensive film cooling. This standard is, however, not realistic when considering service for considerable amount of times ($t > 10\,000 \text{ h}$), since the rapid creep of the TBC at above 900 °C, associated with the great mismatch between its coefficient of thermal expansion (CTE) with the alloy, increase the risk of spallation and limit the use of metal-based components in turbine engines.^[7–10] Especially envisioning the use of carbon-free fuel sources in future gas turbines like hydrogen or ammonia, water vapor is one of the main products of combustion, which intensifies the degradation of these alloys.^[5,11–13] Hence, advances towards reduced greenhouse gas emissions and more efficient gas turbines require their substitution by more robust materials resistant to oxidation and corrosion, which can endure service at higher temperatures.

Due to their reduced density, lower CTE ($3\text{--}5.5 \times 10^{-6} \text{ K}^{-1}$), high temperature creep resistance and melting points, non-oxide silicon based ceramics as Si_3N_4 , SiC, and SiC/SiC composites stand out for application in combustion environments.^[14–21]

1. Introduction

Over the last two centuries, economic growth has been driven at the expense of the environment. In a scenario where the demand for energy constantly grows, fossil fuel-fired power generation still accounts for over 70% of greenhouse gas emissions, caused mainly by the combustion of coal and oil. According to the International Energy Agency, energy-related

M. Lenz Leite, W. Krenkel, S. Schafföner, G. Motz
Department of Ceramic Materials Engineering
University of Bayreuth
Prof.-Rüdiger-Bormann-Str. 1, 95447 Bayreuth, Germany
E-mail: guenter.motz@uni-bayreuth.de
U. Degenhardt
FCT Ingenieurkeramik
Gewerbepark 11, 96528 Frankenblick, Germany

 The ORCID identification number(s) for the author(s) of this article can be found under <https://doi.org/10.1002/admi.202102255>.

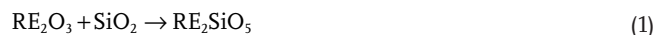
© 2022 The Authors. Advanced Materials Interfaces published by Wiley-VCH GmbH. This is an open access article under the terms of the Creative Commons Attribution License, which permits use, distribution and reproduction in any medium, provided the original work is properly cited.

DOI: 10.1002/admi.202102255

In oxidative environments, the formation of a thermally grown SiO₂ scale ensures an excellent oxidation stability. Nevertheless, H₂O_(v) reacts with this scale at temperatures above 1200 °C, leading to active corrosion and the rapid recession of the ceramic surface. Over the last two decades, progress has been made to develop reliable environmental barrier coatings (EBC) to hinder hot gas corrosion.^[19,22–26] Among the suitable EBC materials, rare-earth silicates have gained attention due to a high temperature endurance of at least 1400 °C and very low SiO₂ volatility.^[10,19,27–29] Despite the higher corrosion rates of the disilicates in comparison with monosilicates, the lower CTE results in a better thermomechanical compatibility to Si₃N₄, SiC, and SiC/SiC substrates. Thus, they are one of the best solutions to design reliable EBCs for gas turbines. Particularly, ytterbium disilicate (Yb₂Si₂O₇, CTE = 4.1 × 10^{−6} K^{−1}) exhibits no polymorphism and is therefore a very attractive EBC candidate.^[27,30,31]

Despite the suitable protection against corrosion, the diffusion of oxygen through the EBC during long-term service at high temperatures leads to the oxidation of the substrate and jeopardizes the mechanical stability of coated systems.^[32,33] Therefore, thermomechanical compatible bond-coats based on mullite (CTE = 5–6 × 10^{−6} K^{−1}) or silicon (CTE = 3.5–4.5 × 10^{−6} K^{−1}) are applied.^[10,27,34–36] Compared to mullite, silicon bond-coats are dense and can effectively hinder the diffusion of oxygen by forming a slow-growing SiO₂ scale (CTE = 3.1 × 10^{−6} K^{−1}, β-cristobalite). Moreover, they have been reported to enhance adhesion, whereas mullite coatings usually exhibit an insufficient bonding strength to non-oxide silicon-based ceramics.^[10,27,37] Among the most common techniques for the deposition of EBC systems onto non-oxide silicon-based ceramics are plasma spray,^[10,27,34,38] chemical^[39,40] or physical vapor deposition,^[20] which are cost intensive and difficult coating procedures for complex shapes. By contrast, slurry-based techniques such as sol-gel or polymer derived ceramics (PDC) enable the deposition of coatings by simple methods as spraying, spin- or dip-coating.^[41–45] Particularly, the PDC route relies on the use of reactive silicon-based polymers as silazanes, carbosilanes, and siloxanes. A thermal treatment after or during the shaping at low temperatures induces cross-linking, resulting in a thermoset, whereas further heating above 400 °C yields ceramic materials. Among the available precursors for coating application, silazanes stand out due to the commercial availability, high ceramic yield, strong adhesion to most substrates, and high stability in oxidative and corrosive media, even at high temperatures.^[41,42,46] The protective effect of silazane-based coatings in such environments is often based on the formation of a passivating SiO₂ scale. However, SiO₂ degrades in combustion environments upon reaction with water vapor. Moreover, mass loss and densification during the polymer to ceramic transition by pyrolysis cause a volume shrinkage exceeding 50%,^[41,47] limiting the achievable thickness of crack and pore-free coatings to only a few micrometers.^[48,49] An approved approach to compensate the precursor shrinkage is the use of fillers, hence enabling the deposition of thicker coatings with tailored properties.^[42,47,48,50–52] These fillers are usually classified as passive, active, and meltable. In contrast to passive fillers, active fillers undergo reaction with the atmosphere, precursor or pyrolysis products, thus expanding in volume and yielding tailored ceramic phases. The main role of meltable fillers is to

act as densifying agents during melting, sealing porosity and relaxing stresses due to CTE mismatches at high temperatures. Consequently, dense silazane-based coatings of up to 100 μm for protection of steel substrates against oxidation and corrosion up to 700 °C were successfully developed.^[51] Moreover, in a previous work^[53] it was demonstrated that silazanes react with rare-earth oxides (RE₂O₃, RE = Y or Yb) as active fillers during pyrolysis in air to yield the respective silicates according to Equations (1) and (2). Due to the shrinkage of the silazane precursor during pyrolysis, crack-free but porous coatings could only be obtained by limiting its amount, whereas the deficit of silicon resulted in unreacted rare-earth oxides.



A similar coating strategy was reported for the generation of ytterbium mono- and disilicates on Si₃N₄ by the reaction of a polysiloxane and Yb₂O₃ during pyrolysis. The Si₃N₄ substrate was coated by dipping, followed by pyrolysis at 1000 °C in air and sintering at 1500 °C in N₂ atmosphere, achieving a coating thickness of 20 μm. However, no information about the formed crystalline phases was provided. Moreover, the coatings rapidly spalled-off during hot gas corrosion tests at 1450 °C for 200 h (*p* = 1 atm, *p*_{H₂O} = 0.18 atm, and *v* = 100 m s^{−1}) due to the residual porosity and insufficient adhesion to the substrate.^[54]

Our goal was to develop a straightforward approach to generate dense, crystalline, and well-adhering Yb₂Si₂O₇ coatings for the protection of non-oxide silicon based ceramics in very harsh combustion environments. The silazane Durazane 1800 was chosen as a binder and a source of silicon to form SiO₂ in oxidative environments, which is essential to convert the active filler Yb₂O₃ to the desired silicate phase. Elemental Si was selected as an additional active filler to provide for a quantitative and stoichiometric Yb₂Si₂O₇ yield. Silicon nitride was employed as the substrate in this study, as it is one of the most promising structural ceramics for the application in gas turbines. To avoid the formation of blisters at the surface of the Si₃N₄ substrate during pyrolysis and densification of the Yb₂Si₂O₇ top-coat in air and improve its adhesion, the development of a bond-coat based on the silazane Durazane 2250 filled with silicon powder was necessary, also ensuring a long-term durability in combustion environments. The thermomechanical stability of the developed Si:Yb(2:1) coating system was assessed by thermal cycling between 1200 and 20 °C and hot gas corrosion at 1200 °C for 200 h with a flow speed of 100 m s^{−1}, thus simulating the very harsh environments in gas turbines.

2. Experimental Section

Figure 1 shows the flowchart of the experimental procedures. Detailed information about each step will be provided in the following sections.

2.1. Si Bond-Coat

Preliminary research with the developed Yb₂Si₂O₇ coatings on Si₃N₄ revealed the limited oxidation stability of the selected

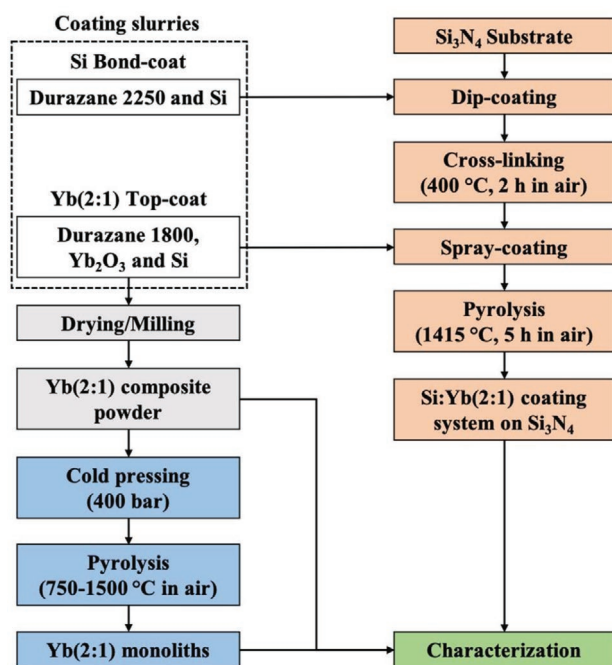


Figure 1. Flowchart of the experimental procedures for the processing of the Yb(2:1) composite powder and monoliths and the Si:Yb(2:1) coating system.

substrates at temperatures above 1400 °C in air due to the diffusion of sintering additives and impurities into the passivating SiO₂ layer, reducing its viscosity and enhancing oxidation.^[56,71,72] The high temperatures necessary to densify the Yb₂Si₂O₇ coatings led to the formation of blisters, which compromised the mechanical stability of the deposited coatings. Therefore, the development of a tailored bond-coat was necessary to prevent the oxidation of the substrate during pyrolysis in air. For this purpose, the perhydropolysilazane Durazane 2250 (Merck KGaA, Germany, **Figure 2**), available in a 20 wt% solution in di-n-butyl ether (DBE), was selected due to the formation of a dense passivating SiO₂ scale to avoid the diffusion of oxygen. Moreover, its high reactivity with moisture favors the formation of chemical Si-O-Substrate bonds with OH groups adsorbed at the surface of metal and ceramic substrates, enhancing the adhesion of coating systems.^[48,49,95] The addition of elemental Si powder grade (AX 05, d50 = 4 μm, Kyocera K. K., Germany) enabled the deposition of thicker coatings, providing an improved oxidation protection of the substrate by the formation of SiO₂ and further densification of the bond-coat during pyrolysis in air. Suitable coating slurry was achieved by stirring elemental Si powder in the Durazane 2250 solution, according to the composition of **Table 1**.

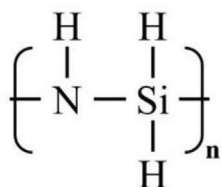


Figure 2. Simplified chemical structure of Durazane 2250.

Table 1. Composition of the Si bond-coat.

Components	wt%
Durazane 2250 ^{a)}	72
Si	28

^{a)}20 wt% solution in DBE.

2.2. Yb(2:1) Top-Coat

For the development of the Yb₂Si₂O₇ EBC, the oligosilazane Durazane 1800 (Merck KGaA, Germany) was used as a binder for the filler particles and as a source of silicon (**Figure 3**). Based on a previous study,^[53] reactive pyrolysis of Durazane 1800 and RE₂O₃ in air yields rare-earth mono or disilicates, depending on the Si:RE₂O₃ ratio. Therefore, Ytterbium(III) oxide (Yb₂O₃) d50 = 200 nm, REacton, 99.9% (REO) (Alfa Aesar GmbH & Co KG, Germany) (**Figure 4a**) was used as an active filler. Elemental Si powder grade AX 05 d50 = 4 μm (Kyocera K. K., Germany, **Figure 4b**) was added to achieve the stoichiometric conversion of Yb₂O₃ to Yb₂Si₂O₇, also acting as an active filler and second source of silica during pyrolysis in air as well as to compensate the shrinkage of the silazane.

The top-coat slurry was prepared by dispersing both fillers in di-n-butyl ether 99+% (Acros Organics BVBA, Belgium) with 4.5 wt% of Disperbyk-2070 (BYK-Chemie GmbH, Germany) as dispersing agent, regarding the used filler mass. ZrO₂ milling beads (Sigmund Lindner GmbH, Germany) with a mean diameter of 2.0 mm were added to the slurry in order to improve the homogeneity and to decrease the mean particle size of the fillers, consequently increasing their surface area and reactivity. Thereafter, a solution of Durazane 1800 and 3 wt% dicumyl peroxide (DCP) (Merck KGaA, Germany) was added to the mixture. DCP acts as an initiator for vinyl polymerization and hydrosilylation reactions, promoting the cross-linking of Durazane 1800 at low temperatures and increasing the ceramic yield during pyrolysis.^[62] Based on the ceramic yield of the oligosilazane after pyrolysis in air at above 1000 °C (81 wt%) and the resulting elemental composition (SiC_{1.15}N_{0.68}O_{0.42}),^[46] a total molar ratio of 2 for Si:Yb₂O₃ was calculated, according to the composition shown in **Table 2**, named Yb(2:1).

2.3. Processing of Powder and Monoliths

2.3.1. Yb(2:1) Composite Powder

In order to acquire information on the formation of the Yb₂Si₂O₇ phase and its sintering behavior, any influence of the

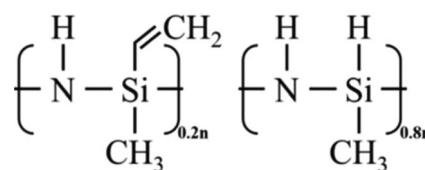


Figure 3. Simplified chemical structure of Durazane 1800.

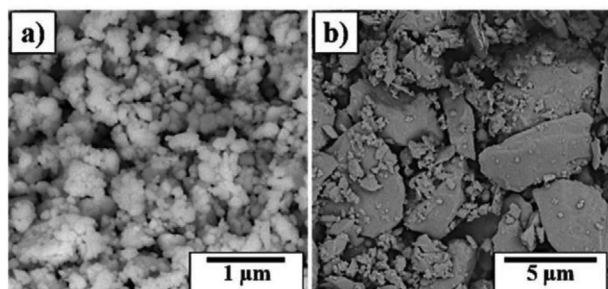


Figure 4. SEM micrographs of the used a) Yb_2O_3 and b) Si powders.

substrate was initially excluded by investigating powder and monolithic samples processed from the Yb(2:1) slurry. Therefore, the solvent was removed from the slurry under stirring and reduced pressure (10^{-2} mbar) at 80 °C for 5 h, followed by milling the dried solid mixture in a vibratory disc mill Pulverisette 9 (Fritsch GmbH, Germany) for 60 s, yielding a homogeneous powder with a decreased particle size.

2.3.2. Cold Pressing of Yb(2:1) Monoliths

The processing of monoliths with approximate dimensions of $\varnothing 12 \times 3$ mm was carried out by uniaxially pressing the Yb(2:1) composite powder at 40 MPa, followed by pyrolysis in air at 750 °C, from 900 to 1300 °C in 100 K steps and at 1415 °C for 1 h in an HT04/18 chamber furnace (Nabertherm GmbH, Germany). In order to investigate microstructural and composition changes at increased annealing times and temperatures, two additional monoliths were pyrolyzed at 1415 and 1500 °C for 5 h in air.

2.4. Deposition of the Si:Yb(2:1) Coating System

For the deposition of the coating system, Si_3N_4 substrates SNPU (FCT Ingenieurkeramik GmbH, Germany) were selected due to the low sintering additive content, composed of a mixture of Y_2O_3 , MgO, and Al_2O_3 . Before the coating application, the $30 \times 25 \times 5$ mm³ Si_3N_4 substrates were cleaned in an acetone ultrasound bath for 25 min in order to remove any surface impurities, which may hinder the adhesion of the coating. The cleaned Si_3N_4 substrates were then dip-coated into the Si bond-coat slurry using a RDC 10 dip-coater (Bungard Elektronik GmbH & CO. KG, Germany) with a hoisting speed of 0.5 m min⁻¹. The coated substrates were dried and cross-linked at 400 °C for 2 h in air in order to yield a stable thermoset bond-coat. The Yb(2:1) slurry was then applied as the top-coat by spraying, using a 781S spray gun (Nordson Deutschland GmbH,

Germany). Pyrolysis was carried out at 1415 °C for 5 h in air (see Section 3.2). The resulting coating system was named Si:Yb(2:1), whereby Si designates the Si bond-coat and Yb(2:1) the top-coat.

2.5. Characterization Methods

2.5.1. Pyrolysis Behavior of the Yb(2:1) Composite Powder

The pyrolysis behavior and mass change of the Yb(2:1) composite powder and of the respective slurry components listed in Table 2 were investigated by thermogravimetric analysis (TGA) in a STA 449 F5 Jupiter (Netzsch GmbH & Co. Holding KG, Germany) up to 1415 °C at 5 K min⁻¹ and annealing for 5 h in synthetic air (80/20 vol% N_2/O_2).

2.5.2. Composition and Microstructure of the Yb(2:1) Monoliths

Details about the resulting microstructure and composition of the pressed Yb(2:1) monoliths after pyrolysis in air in the range between 750 and 1500 °C were analyzed by scanning electron microscopy (SEM, Gemini Sigma 300 VP, Carl Zeiss AG, Germany), coupled with an EDAX Octane Elect Silicon Drift Detector (SDD), used for energy-dispersive X-ray spectroscopy (EDS). The corresponding crystalline phase formation was investigated by X-ray diffractometry (XRD) in a D8 ADVANCE (Bruker AXS, Germany) using monochromatic $\text{CuK}\alpha$ radiation. For XRD analysis, the monoliths were grinded in the Pulverisette 9 mill for 60 s to yield a more accurate signal from the crystalline phases within the respective samples. The resulting diffractograms were evaluated with the PDF-4+ 2020 structural database. The density and open porosity content of the pyrolyzed monoliths was measured by helium pycnometry (Accupyc II 1340, Micromeritics Instrument Corporation, USA). Their true density was determined by grinding the corresponding pyrolyzed monolith and measuring the resulting powder by helium pycnometry.

2.5.3. Properties of the Si:Yb(2:1) Coating System on Si_3N_4

The microstructure and composition of the Si:Yb(2:1) coating system on Si_3N_4 after pyrolysis was analyzed by SEM and EDS as described in detail in Section 2.5.2. Information on the open porosity content was obtained by converting the respective SEM micrographs of the surface of the coating system into a binary image and quantifying the porosity using the software ImageJ.^[96] The crystalline phases were analyzed by XRD measurements of the surface of the coated samples. The adhesion strength of the coating systems was measured by pull-off tests using a PosiTest AT-A (DeFelsko Corporation, USA), according to the ASTM D4541. Therefore, $\varnothing 10$ mm dollies were glued onto the surface of the coated samples with a two-component epoxy resin Loctite EA 9466 (Henkel Central Eastern Europe GmbH, Austria). The resin was cured at 110 °C for 1 h in air, before the dollies were pulled perpendicularly with a constant force of 1 MPa s⁻¹ and the tensile strength necessary to detach them was recorded. The values reported herein are an average

Table 2. Composition of the Yb(2:1) top-coat.

Component	wt%
Durazane 1800 + 3 wt% DCP	3
Yb_2O_3	86
Si	11

of three measurements. The failure mechanism was examined by SEM/EDS analysis. Microhardness measurements were performed by using a Fischerscope H100 (Helmut Fischer GmbH, Germany) and an applied maximal load of 981 mN (HV 0.1) at the surface of the coated samples, achieving a maximal depth corresponding to 1/10 of the coating thickness, according to the standard DIN EN ISO 14 577. The load necessary to damage the surface of the coatings was determined by a scratch tester (Linearterster 249, Erichsen GmbH & Co. KG, Germany) with varying load ranging from 5 to 40 N. Therefore, a testing rod 15/570 (\varnothing 1.0 mm) was used, according to the standard ISO 1518-1 and the induced scratches on the coatings were examined by optical microscopy (Axiotech HAL 100, Carl Zeiss AG, Germany).

The thermal cycling stability of the Si:Yb(2:1) coating system on Si_3N_4 was evaluated by placing coated samples in a N41/H chamber furnace (Nabertherm GmbH, Germany) pre-heated at 1200 °C and annealing them for 1 h, before quenching in a water bath at 20 °C. After each cycle, the samples were allowed to dry at 110 °C for 30 min in a Nabertherm LE 14/11 chamber furnace before carrying the test on. A total of 15 cycles were performed. Finally, the potential of the developed coating system for application in gas turbines was assessed by technical hot gas corrosion, carried out at Fraunhofer-Institut für Keramische Technologien und Systeme (IKTS, Dresden, Germany). Hence, $35 \times 4 \times 3 \text{ mm}^3$ Si_3N_4 substrates were completely coated according to the procedure described in Section 2.4. The resulting samples were placed inside an Al_2O_3 tube furnace, followed by hot gas corrosion at 1200 °C for 200 h in moist air atmosphere ($p = 1 \text{ atm}$, $p_{\text{H}_2\text{O}} = 0.15 \text{ atm}$, and $v = 100 \text{ m s}^{-1}$). After 125 h, the $p_{\text{H}_2\text{O}}$ was reduced from 0.15 to 0.08 atm. In order to determine the mass change, their mass was recorded after pyrolysis and at the time intervals of 25, 75, 125, and 200 h. For this purpose, the tube furnace was cooled down to room temperature and the weight of the samples was measured, before progressing the test. The mass change reported in this work is an average value obtained from a pair of identical samples. As reference, uncoated Si_3N_4 substrates were likewise corroded.

3. Results and Discussion

3.1. Pyrolysis Behavior of the Yb(2:1) Composite Powder

In order to understand the behavior of the Yb(2:1) composite material during the thermal treatment applied for the synthesis and sintering of the $\text{Yb}_2\text{Si}_2\text{O}_7$ phase, thermogravimetric analysis was performed up to 1415 °C with a subsequent annealing of 5 h in air. The mass change as a function of the temperature and annealing time at 1415 °C of the Yb(2:1) composite and each individual component (see Table 2, Section 2.2) is displayed in Figure 5.

As expected, TG analysis confirmed the stability of ytterbium oxide up to 1415 °C in air. By contrast, the oxidation of the elemental Si particles began at ≈ 750 °C in air by the formation of an amorphous and dense SiO_2 scale.^[55–61] The passive oxidation of elemental Si is limited by the inward diffusion of oxygen through the forming SiO_2 scale, exhibiting a parabolic rate at constant temperatures, which increases linearly with a rising temperature.^[55] This explains the rapid mass gain of 25 wt% detected up to 1415 °C and the final yield of $\approx 128 \text{ wt}\%$ after further annealing at 1415 °C for 5 h in air, corresponding to a conversion of 25 mol% of Si to SiO_2 . The oligosilazane Durazane 1800 underwent a total mass loss of $\approx 19 \text{ wt}\%$ up to ≈ 750 °C, but then remained stable up to 1415 °C. According to previous studies,^[46,62,63] the mass loss up to 200 °C can be attributed to the volatilization of low molecular weight oligomers. The following mass loss up to 400 °C resulted from the release of NH_3 , H_2 and their respective oxidation products. However, the incorporation of oxygen induces the formation of Si–O–Si bonds and a higher degree of cross-linking, thus increasing the ceramic yield during pyrolysis. At above 400 °C, the elimination of the organic groups results in a further mass loss of up to ≈ 750 °C. Nevertheless, the formation of a passivating SiO_2 layer hindered the diffusion of oxygen and the complete elimination of C and N. Hence, a predominantly amorphous ceramic with an approximate molar composition of $\text{Si}_{1.15}\text{N}_{0.69}\text{O}_{0.41}$ was obtained after pyrolysis at 1600 °C in air.^[46]

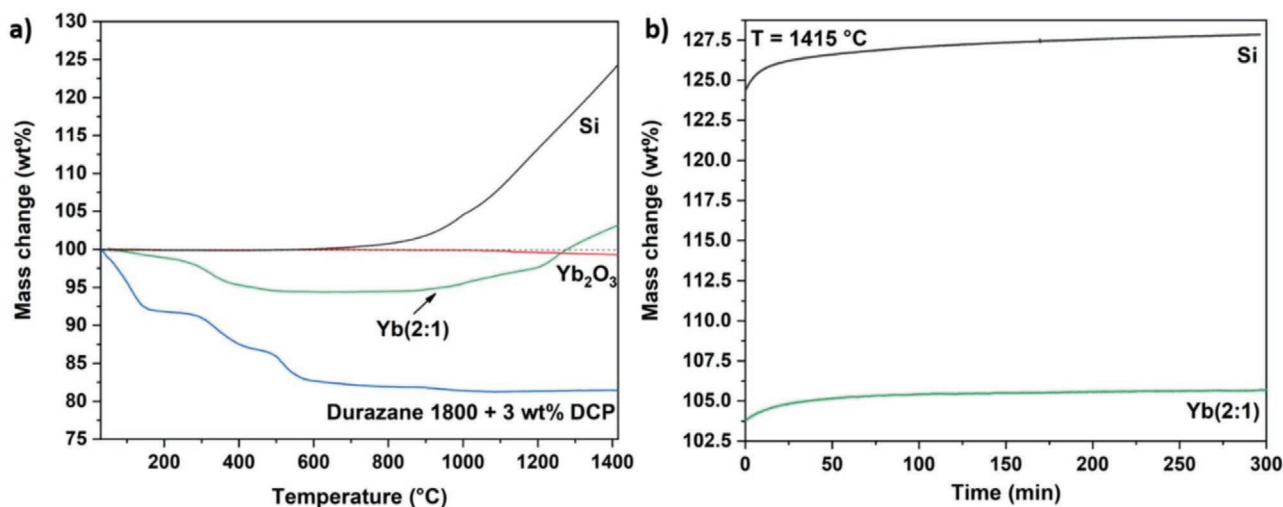


Figure 5. a) Thermogravimetric analysis of the individual components and the Yb(2:1) composite powder up to 1415 °C at 5 K min⁻¹ and b) annealing up to 5 h at 1415 °C in synthetic air.

Unlike for Durazane 1800 + 3 wt% DCP, the decomposition of the Yb(2:1) composite powder started at ≈ 100 °C, which was possibly caused by the drying step carried out at 80 °C for 5 h under reduced pressure (see Section 2.3.1), leading to the volatilization of oligomers before the TG measurement. Afterwards, the resulting mass loss of 6 wt% up to 750 °C was attributed to the further pyrolysis of the silazane as described above. Beyond this temperature, the oxidation of the Si powder started and the formation of SiO₂ was responsible for the mass gain, achieving a yield of 103 wt% at 1415 °C. Further annealing at this temperature for another 5 h exhibited a similar trend as measured for elemental Si under the same conditions, denoted by a parabolic oxidation rate. Hence, a slight mass gain of 3 wt% was measured, resulting in a maximum yield of ≈ 105 wt%. By considering the composition provided in Table 2, the final mass changes of the individual components, a theoretical yield of 97 wt% should be achieved. Nevertheless, the complete oxidation of Durazane 1800 and Si to SiO₂ would lead to a yield of 107 wt%, which was in good agreement with the measurement displayed in Figure 5. It is important to note that in both estimated theoretical yields, the complete elimination of the dispersing agent was considered. Hence, the TG measurement provides evidence for a higher reactivity of the Durazane 1800 and Si with oxygen from the atmosphere in the presence of Yb₂O₃. This result confirms the hypothesis of Lenz Leite et al.^[53] that the solid-state reaction between Durazane 1800 and Yb₂O₃ led to nearly the quantitative yield of the respective silicates at temperatures above 1400 °C in air, whereas no residual carbide or nitride phases were detected at this temperature.

3.2. Composition and Microstructure of the Yb(2:1) Monoliths

The analysis of the microstructure and composition of the Yb(2:1) monoliths after pyrolysis allowed the study of the

formation of the Yb₂Si₂O₇ phase and its sintering behavior without the influence of the selected Si₃N₄ substrate, whereby the ideal temperature for the conversion and densification of the Si:Yb(2:1) coating system was determined. Due to the similar microstructure and composition of the monoliths pyrolyzed between 750 and 900 °C, 1200 and 1300 °C as well as 1415 and 1500 °C, only the temperature ranges from 900 to 1100 °C and from 1300 to 1415 °C will be discussed in detail. Figure 6 shows the respective XRD diffractograms.

At 900 °C, the detection of crystalline Yb₂O₃ and Si as the only present phases indicated that no reaction to ytterbium silicate phases took place. Nevertheless, at 1000 °C the peaks associated with elemental Si disappeared. This is likely a consequence of its oxidation, supported by the detection of α -cristobalite as well as the incipient formation of ytterbium silicates, reducing the fraction of elemental Si. Despite the considerable amounts of Yb₂O₃, the solid-state reaction of Yb₂O₃ with the newly formed SiO₂ resulted in β -Yb₂Si₂O₇ and the metastable phase of monoclinic P21/c Yb₂SiO₅. In addition, peaks corresponding to secondary phases as ytterbium nitrogen silicates, carbides, and silicides were identified, which resulted from reactions of the pyrolysis products of the oligosilazane and elemental Si with Yb₂O₃. However, the broadness of the detected signals hindered the accurate assignment of these phases, which also indicated a low degree of crystallinity. After annealing at 1100 °C for 1 h, the peaks related to the secondary phases disappeared due their low stability in air at high temperatures, forming the respective oxide and silicates.^[53,64] The further consumption of Yb₂O₃ led to the formation of β -Yb₂Si₂O₇ and Yb₂SiO₅, which were already the main crystalline phases. At this temperature, the transition of the metastable P21/c Yb₂SiO₅ into the equilibrium monoclinic I2/a Yb₂SiO₅ phase was also confirmed, which is in agreement with reported results.^[65,66] At higher temperatures, XRD analysis evidenced the slow conversion of the monosilicate phase to

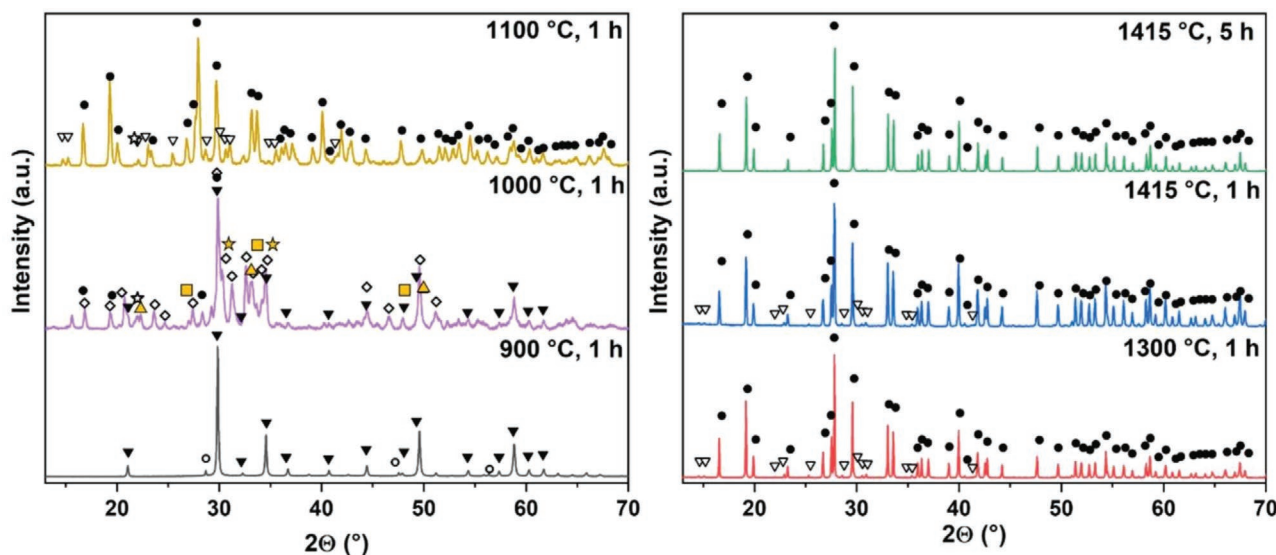


Figure 6. XRD analysis of the Yb(2:1) pressed monoliths after pyrolysis in air at different temperatures and annealing times (\blacktriangledown – Yb₂O₃ (04-001-2438); \bullet – Si (00-027-1402); \star α -cristobalite (00-039-1425) \diamond – P21/c Yb₂SiO₅ (00-052-1187); ∇ – I2/a Yb₂SiO₅ (00-040-0386); \bullet – β -Yb₂Si₂O₇ (00-025-1345); \triangle – Yb₆Si₁₁N₂₀O (04-010-8242); \square – Yb₄Si₇ (04-013-6752); \star – Yb₃C₄ (04-003-2283)).

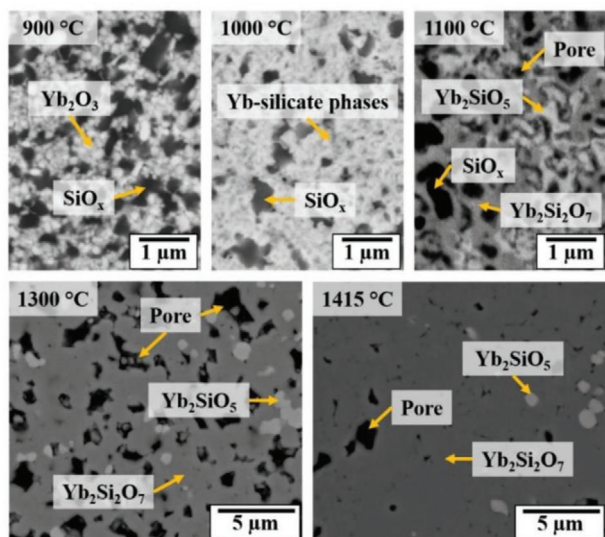


Figure 7. SEM micrographs of the cross-section of the Yb(2:1) monoliths after pyrolysis at 900, 1000, 1100, and 1300 °C for 1 h and at 1415 °C for 5 h in air.

the disilicate. Hence, only traces of Yb_2SiO_5 are still detected after pyrolysis at 1300 °C, which remained up to 1415 °C. Nevertheless, by annealing the monolith at 1415 °C for another 5 h, the XRD analysis indicated the stoichiometric conversion of Yb_2O_3 , Si and Durazane 1800 to $\beta\text{-Yb}_2\text{Si}_2\text{O}_7$. The following SEM/EDS analysis of the corresponding monoliths revealed additional information about their conversion to $\beta\text{-Yb}_2\text{Si}_2\text{O}_7$ and the sintering behavior of this phase as a function of the temperature (Figure 7).

After pyrolysis at 900 °C for 1 h, the visible white and black regions corresponded to the initially used Yb_2O_3 and Si particles, respectively. In comparison with Figure 4b, the use of ZrO_2 milling beads during the slurry preparation (see Section 2.2) reduced the mean particle size of the elemental Si powder from $\approx 4 \mu\text{m}$ to less than $1 \mu\text{m}$. EDS analysis of the Si particles detected a non-stoichiometric amount of oxygen relative to the silica phase, which indicates an initial stage of oxidation in accordance with TG and XRD measurements. These particles were marked as SiO_x . At 1000 °C, the fraction of SiO_x and Yb_2O_3 decreased substantially, which can be directly correlated with the formation of ytterbium silicate phases, denoted by the light grey regions, also confirming XRD measurements. Due to the difficult detection and quantification of carbon and nitrogen by SEM/EDS analysis, the presence of secondary phases such as ytterbium carbide, silicide, or nitrogen silicate phases could not be confirmed after pyrolysis at 1000 °C, as otherwise indicated by XRD. At 1100 °C, Yb_2SiO_5 and $\text{Yb}_2\text{Si}_2\text{O}_7$ were already well-defined phases, whereby the latter phase was predominantly detected near the SiO_x particles and is characterized by a compact microstructure. According to XRD and TG analyses, the formation of $\text{Yb}_2\text{Si}_2\text{O}_7$ is almost concluded at 1300 °C. Hence, only traces of remaining Yb_2SiO_5 were detected by SEM/EDS, which were embedded in an $\text{Yb}_2\text{Si}_2\text{O}_7$ matrix. Even so, remaining amounts of Yb_2SiO_5 were determined after pyrolysis at 1415 °C for 5 h. In this case, the marginal relative concentration of this phase compared to $\text{Yb}_2\text{Si}_2\text{O}_7$ could have

Table 3. Open porosity measurements and overview of the phase formation of the Yb(2:1) monoliths after pyrolysis in air.

Temperature	Open porosity [vol%]	Detected phases
900 °C, 1 h	33	Yb_2O_3 , Si, SiO_2
1000 °C, 1 h	32	Yb_2O_3 , Si, SiO_2 , Yb_2SiO_5 (P21/c), $\beta\text{-Yb}_2\text{Si}_2\text{O}_7$, $\text{Yb}_3\text{C}_4^{\text{a}}$, $\text{Yb}_4\text{Si}_7^{\text{a}}$, $\text{Yb}_6\text{Si}_{11}\text{N}_{20}\text{O}^{\text{a}}$
1100 °C, 1 h	33	SiO_2 , Yb_2SiO_5 (I2/a), $\beta\text{-Yb}_2\text{Si}_2\text{O}_7$
1300 °C, 1 h	17	Yb_2SiO_5 , $\beta\text{-Yb}_2\text{Si}_2\text{O}_7$
1415 °C, 1 h	5	Yb_2SiO_5 , $\beta\text{-Yb}_2\text{Si}_2\text{O}_7$
1415 °C, 5 h	4.5	Yb_2SiO_5 , $\beta\text{-Yb}_2\text{Si}_2\text{O}_7$

^a) Detected by XRD, but not confirmed by SEM/EDS analysis.

prevented its detection by XRD. Table 3 lists the phases detected by XRD and SEM/EDS analyses and displays the results of the open porosity content of the Yb(2:1) monoliths after pyrolysis, which was calculated based on the respective apparent volume and helium pycnometry measurements.

Before pyrolysis, an open porosity of 22 vol% was measured for the pressed monoliths, which increased to 33 vol% after pyrolysis at 900 °C. However, no pores were detected by SEM analysis (Figure 7), which were homogeneously distributed and too small for the used resolution. As confirmed by TG analysis (refer to Figure 5), the formation of porosity up to 900 °C is primarily a consequence of the mass loss and shrinkage of Durazane 1800 during the polymer to ceramic transition. Nevertheless, the oxidation of the Si particles was accompanied by a molar volume expansion by a factor of 2.2, which can partially compensate the shrinkage of the silazane up to 900 °C reducing the porosity.^[55–61] Despite the formation of ytterbium silicate and secondary phases above 1000 °C, no apparent change in the porosity content was measured up to 1100 °C, which remained constant at ≈ 33 vol%. In this regard, the formation of $\beta\text{-Yb}_2\text{Si}_2\text{O}_7$ (6.15 g cm^{-3})^[67] and I2/a- Yb_2SiO_5 (7.28 g cm^{-3})^[31] phases from Yb_2O_3 (9.17 g cm^{-3})^[31] and SiO_2 (α -cristobalite, 2.33 g cm^{-3})^[68] should lead to a volume shrinkage of up to 11.5%, by considering the total volume of Yb_2O_3 and α -cristobalite before and after the stoichiometric conversion in ytterbium mono- or disilicate. By contrast, the phase transition from P21/c Yb_2SiO_5 to I2/a Yb_2SiO_5 and the oxidation of the secondary phases at 1100 °C, as confirmed by XRD, are reported to be accompanied by a large volume expansion.^[53,65,66] Thus, the constant volume of open porosity may be a consequence of reactions leading to a concurrent volume expansion and shrinkage. The mentioned reactions and phase transition resulted in a coarsened microstructure and larger pores at above 1000 °C. The increasing sintering effects at 1300 °C led to a reduction of the open porosity to 17 vol%. This was supported by SEM micrographs (Figure 7), as the clearly visible pores had a mean size of $\approx 1 \mu\text{m}$. The thermal treatment of the monoliths at 1415 °C for 1 h resulted in a remarkable densification due to the strongly reduced open porosity of only 5 vol%. Further annealing at this temperature for 5 h reduced the open porosity to 4.5 vol%. Without considering the open porosity, the monolith had a density of 5.95 g cm^{-3} , which corresponded to 96% of its density after milling and is comparable to the bulk density of the $\beta\text{-Yb}_2\text{Si}_2\text{O}_7$ phase (6.15 g cm^{-3}).^[67]

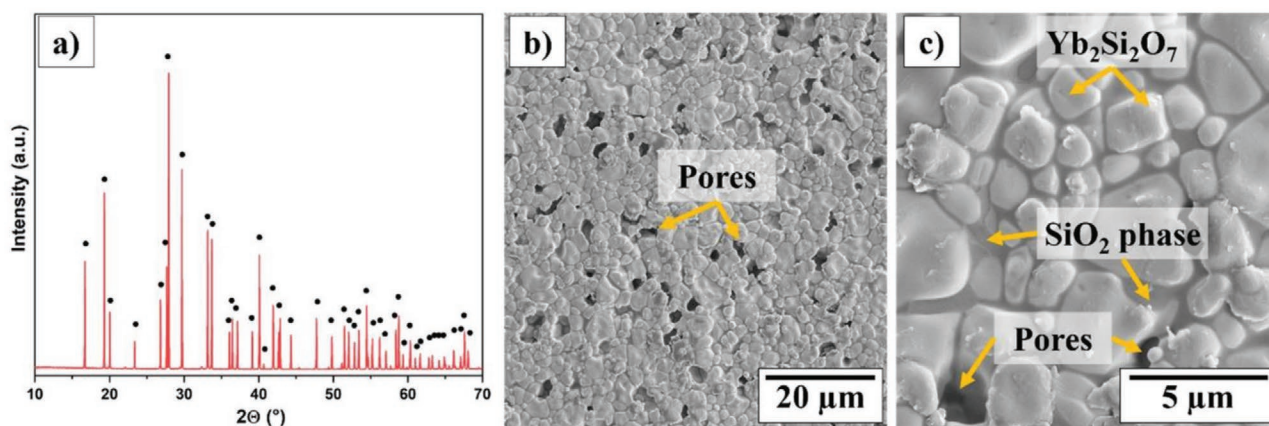


Figure 8. a) XRD diffractogram and b,c) SEM micrograph of the surface of the Si:Yb(2:1) coating system on Si_3N_4 after pyrolysis at 1415 °C and 5 h in air (● – $\beta\text{-Yb}_2\text{Si}_2\text{O}_7$ (00-025-1345)).

Therefore, a closed porosity of 4 vol% was measured for the monolith, resulting in a total porosity content of 8.5 vol%. This value was considerably lower than reported by Wang et al. for the synthesis and sintering of $\beta\text{-Yb}_2\text{Si}_2\text{O}_7$ monoliths.^[69] In their work, the authors prepared a sol-gel containing Yb_2O_3 powder and tetraethoxysilane (TEOS) in a mol ratio of 2 (TEOS: Yb_2O_3), which was then dried at 200 °C for 2 h and pressed at 30 MPa. The pressed monoliths were pyrolyzed at 1550 °C for 4 h in air, yielding single phase $\beta\text{-Yb}_2\text{Si}_2\text{O}_7$. The samples were subsequently milled and screened through a 200-mesh sieve. The resulting $\beta\text{-Yb}_2\text{Si}_2\text{O}_7$ powder was further cold pressed at 240 MPa and sintered between 1300 and 1550 °C for 4 h in air. After sintering at 1400 °C, an open porosity of 29.5 vol% was obtained, whereas sintering at 1500 °C led to an open porosity of 11.3 vol% and a density of 5.25 g cm⁻³. As previously mentioned, in our work a thermal treatment at 1500 °C for 5 h did not result in significant microstructural changes compared to pyrolysis at 1415 °C. Due to the low residual amount of the Yb_2SiO_5 phase and the strongly reduced porosity, pyrolysis at 1415 °C for 5 h in air was selected for the later processing and densification of the Si:Yb(2:1) coating system.

3.3. Properties of the Si:Yb(2:1) Coating System on Si_3N_4

After determining the pyrolysis parameters based on the formation of the $\text{Yb}_2\text{Si}_2\text{O}_7$ phase and the porosity content, Si_3N_4 substrates were coated with the Yb(2:1) slurry and pyrolyzed at 1415 °C for 5 h in air. As previously mentioned in Section 3.2, the coating material was very porous up to 1300 °C. This led to the enhanced oxidation of the selected Si_3N_4 substrate by forming blisters before the densification of the coating. Therefore, the deposition of the bond-coat composed of Durazane 2250 and elemental Si powder prior to the Yb(2:1) coating was necessary to protect the substrate against oxidation. The resulting Si:Yb(2:1) coating system was pyrolyzed at 1415 °C for 5 h in air. XRD analysis of the surface of the coating system on Si_3N_4 substrates (Figure 8a) showed the formation of $\beta\text{-Yb}_2\text{Si}_2\text{O}_7$ as the only crystalline phase, which was in excellent agreement with the corresponding monolithic sample (Figure 6). This also applies to the results of the SEM/EDS analysis of the surface

of the Yb(2:1) top-coat, revealing a dense microstructure with an open porosity content of only 4 vol%, estimated by image analysis using the software ImageJ (Figure 8b). However, at higher magnifications (Figure 8c) round shaped grains with up to 5 μm in diameter and a binder phase could be distinguished, which were characterized by a different elemental composition.

The composition of the grain phase corresponded to $\text{Yb}_2\text{Si}_2\text{O}_7$ as 60 at% O, 19 at% Si, and 21 at% Yb were detected by EDS spot analysis, whereas the binder phase consisted of SiO_2 (26 at% Si and 62 at% O). However, trace impurities of Ca, Mg, Na, and Al were also detected, accounting respectively for less than 4 at%. The absence of crystalline peaks of SiO_2 in Figure 8a indicated its amorphous character.

The SEM analysis of the cross-section of the Si:Yb(2:1) coating system showed well-adherent layers with a thickness of ≈68 μm (Figure 9a). The EDS mappings of N and Yb (Figure 9b) allowed the distinction between the different layers, whereby the thickness of the Yb(2:1) top-coat corresponded to 58 μm. The Si bond-coat was 10 μm thick and consisted only of Si and O. By comparing the Si and O mappings, it was evident that the elemental Si melted within the bond-coat during pyrolysis, densifying its microstructure and effectively protecting the Si_3N_4 substrate against oxidation and the formation of blisters at high temperatures.

The black spots, which were mainly visible at the surface region of the Yb(2:1) top-coat (see Si mapping, Figure 9b), indicated pores within the coating system. By contrast, the amorphous SiO_2 phase was predominantly observed at the bond-coat and at the grain boundaries of the $\text{Yb}_2\text{Si}_2\text{O}_7$ phase, identified by the higher intensities of Si and O, which is in agreement with SEM/EDS analysis of the surface of the coating system (Figure 8c). EDS spot analysis of this phase in the cross-section of the Yb(2:1) coating also confirmed the presence of stoichiometric SiO_2 . The SiO_2 was formed by the oxidation of the elemental Si particles during pyrolysis in air and marked as SiO_2 in Figure 9a. SiO_2 was also detected within the bond-coat, especially at the interfaces to the Si_3N_4 substrate and to the Yb(2:1) coating, encapsulating elemental Si (compare Si and O mappings). This indicates the slight oxidation of the bond-coat/ Si_3N_4 substrate interface during pyrolysis, which could explain the origin of the amorphous SiO_2 phase.

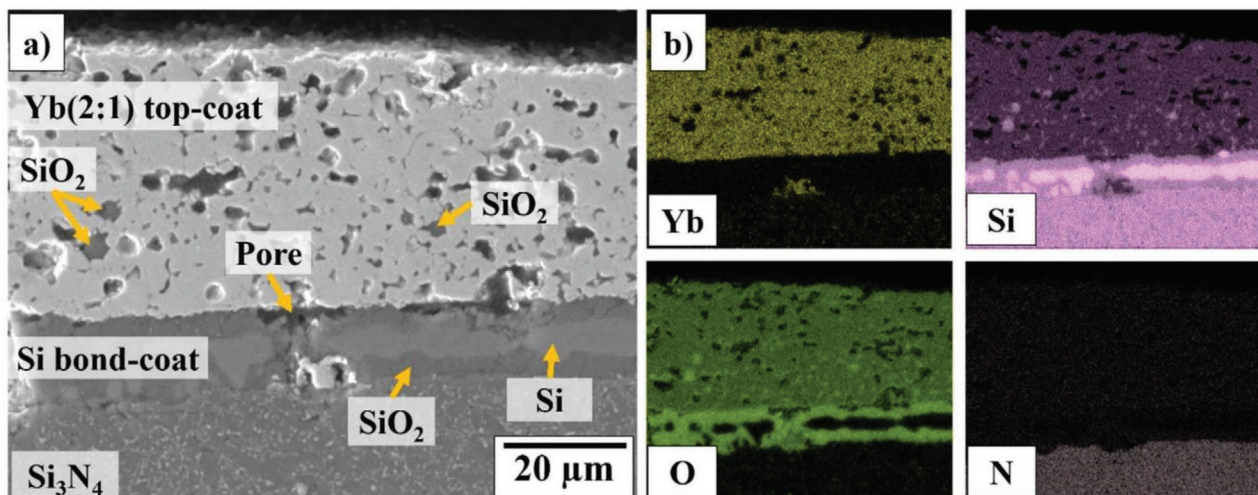


Figure 9. a) SEM micrograph and b) EDS mapping of elements of the cross-section of the Si:Yb(2:1) coating system on Si_3N_4 after pyrolysis at $1415\text{ }^\circ\text{C}$ and 5 h in air.

As discussed in Section 3.2, the densification of the coating system occurred only at $1415\text{ }^\circ\text{C}$. Before a dense microstructure was achieved, the oxidation of the interface between the bond-coat/ Si_3N_4 substrate led to the formation of a passivating SiO_2 layer. The Si_3N_4 substrate contained Y_2O_3 , MgO , and Al_2O_3 as sintering aids. The concentration gradient between cations of these oxides and impurities in the glassy grain boundary phase within the bulk of the Si_3N_4 substrate and the formed passivating SiO_2 layer creates a driving force for their diffusion until equilibrium is reached. By acting as network modifiers, the cation impurities reduce the viscosity of the SiO_2 layer.^[16,17,19,70–75] Especially Ca^{2+} and Mg^{2+} can remarkably reduce the softening temperature of silica-based glasses to $1100\text{--}1300\text{ }^\circ\text{C}$.^[72,76–78] The low viscosity of the generated glassy silica phase favored the infiltration of the coating system, which resulted in a denser microstructure in deeper regions. In comparison with the corresponding monolith (Figure 7), the additional SiO_2 contributed to the conversion of residual Yb_2SiO_5 to $\text{Yb}_2\text{Si}_2\text{O}_7$. This explains the unreacted SiO_2 within the Yb(2:1) top-coat in Figure 9a and the accumulation of glassy SiO_2 at the grain boundaries of $\text{Yb}_2\text{Si}_2\text{O}_7$. The small amounts of cation impurities may still induce the crystallization of SiO_2 at above $1000\text{ }^\circ\text{C}$ in dry atmospheres, whereas the associated volume shrinkage and the subsequent transformation from β to α cristobalite at $270\text{ }^\circ\text{C}$ during cooling may cause the formation of cracks.^[55,68,79–82]

The good mechanical properties of the coating system benefited from the strong interaction of the Si:Yb(2:1) with the Si_3N_4 substrate and from the unexpected infiltration by the glassy SiO_2 phase. Pull-off tests carried out according to the ASTM D4541 confirmed an adhesion strength of $36.9 \pm 6.2\text{ MPa}$, higher than reported for other ytterbium disilicate EBCs/Si bond-coated systems for SiC ($29.1 \pm 0.8\text{ MPa}$).^[83] This result is attributed to the outstanding adhesion between the silazane-based Si bond-coat and the Si_3N_4 substrate.^[34,83–85] In addition, the infiltration with glassy SiO_2 also contributed to the adhesion of the coating system by mechanical anchoring. The failure mechanism was analyzed in detail by SEM/EDS (Figure 10a,b), where C and Al

mappings represent the resin and the aluminum dolly counterpart used in the test, respectively.

The absence of Yb and the concurrently detected high intensities of Si and O at the surfaces of the tested sample and the Al dolly, confirmed that the bond-coat failed by cohesion. This was likely favored by the presence of small defects within it (see Figure 9a). Microhardness measurements at the surface of the coating system yielded hardness values of $713 \pm 169\text{ (HV 0.1)}$ ($6.9 \pm 1.6\text{ GPa}$). The high values were comparable to the intrinsic hardness of $\text{Yb}_2\text{Si}_2\text{O}_7$ ($73 \pm 0.2\text{ GPa}$)^[67] and are also an indication of the low residual porosity content and the dense microstructure of the coating system. To complete the mechanical investigations, scratch tests demonstrated that a critical load of 28 N was necessary to damage the coating system. Light microscopy analysis of the damaged area revealed the typical behavior of well-adhered hard coatings on hard substrates,^[86,87] since plastic deformation was minimal and fracture dominated the scratch response, thus leading to spallation and the formation of wedges (Figure 10c).

Very harsh thermal shock tests between 1200 and $20\text{ }^\circ\text{C}$ (see Section 2.5.3) proved the excellent compatibility between the Si:Yb(2:1) coating system and the Si_3N_4 substrate (Figure 11).

Due to the extreme temperature gradient by quenching the tested sample in a water bath at $20\text{ }^\circ\text{C}$, macroscopic cracks were already formed in the Si_3N_4 substrate after the second cycle, which did not influence the adhesion of the coating system. Hence, it remained completely adhered up to six thermal cycles, whereas only few spallation spots occurred at the edges of the coated Si_3N_4 substrate after 15 cycles, indicated by the yellow arrows (Figure 11). Besides the good CTE compatibility between the coating system and the Si_3N_4 substrate (Si_3N_4 , $\text{CTE} = 3.60 \times 10^{-6}\text{ K}^{-1}$,^[19] Si, $\text{CTE} = 3.5\text{--}4.5 \times 10^{-6}\text{ K}^{-1}$,^[10] SiO_2 (β -cristobalite), $\text{CTE} = 3.1 \times 10^{-6}\text{ K}^{-1}$,^[27] β - $\text{Yb}_2\text{Si}_2\text{O}_7$, $\text{CTE} = 4.1 \times 10^{-6}\text{ K}^{-1}$ ^[19]), the excellent performance during thermal shock tests was also associated with the well distributed residual porosity within the coating and with the softening of the glassy SiO_2 phase at high temperatures. The residual porosity decreased the Young's modulus of the coating, thus increasing its thermal shock tolerance, whereas the

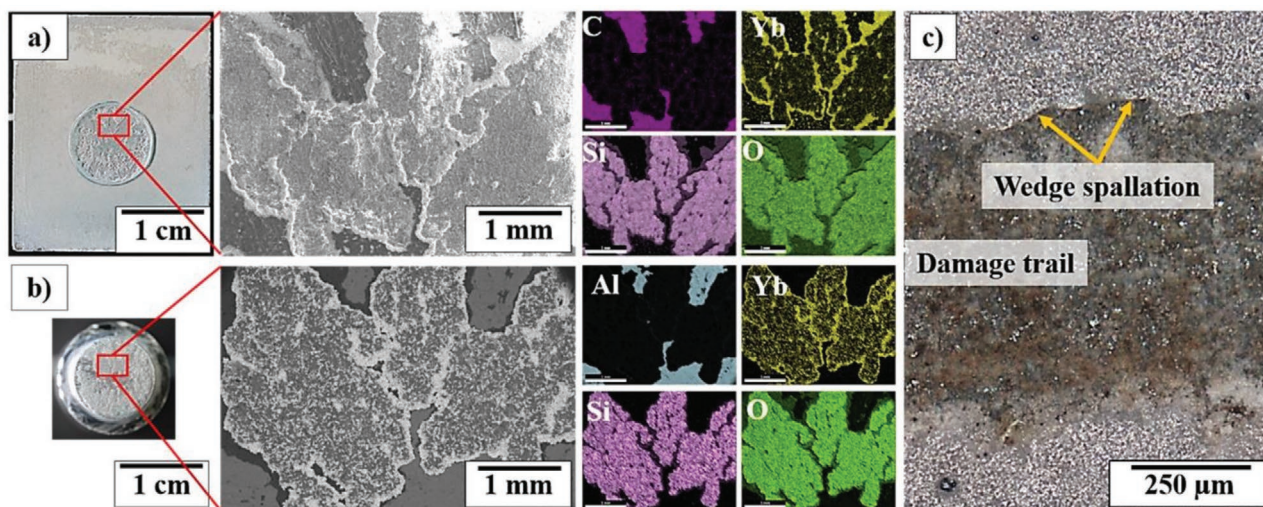


Figure 10. Photo and respective SEM/EDS micrographs of a) Si:Yb(2:1) coating system on Si_3N_4 and b) Al dolly counterpart after pull-off test. c) Light microscopy analysis of the surface of the Si:Yb(2:1) coating system after scratch tests (applied load: 28 N).

softening of the glassy SiO_2 phase during annealing at 1200 °C likely led to the relaxation of stresses generated upon thermal cycling.^[88,89]

Finally, the Si:Yb(2:1) coating system was tested in extreme hot gas corrosion atmospheres simulating conditions in gas turbines, comparing its performance with the uncoated Si_3N_4 substrates. **Figure 12** displays photos of the samples before and after the hot gas corrosion test. After exposure at 1200 °C for 200 h and a gas flow speed of 100 m s^{-1} , the surface of the uncoated samples acquired a white and opaque color, indicating the formation of an oxidation layer (samples 1 and 2). On the other hand, the coated samples appeared intact and the coating system remained adhered to the Si_3N_4 substrate (samples 3 and 4). The specific mass loss over time and XRD analysis of the corroded samples are shown in **Figure 13**.

As expected, the high flow rate led to the rapid degradation of the Si_3N_4 substrates in hot gas environments at 1200 °C. However, the corrosion rate of the coated Si_3N_4 samples was substantially reduced by 96% after 200 h under these very harsh conditions. In combustion environments, corrosion, oxidation, and convective mass transfer occur simultaneously and contribute simultaneously to the mass change. In this case, the mass loss measured for both uncoated and coated Si_3N_4 substrates after 200 h indicated the predominance of corrosion reactions. The decrease in the corrosion rate over time

was already noticeable for the uncoated Si_3N_4 substrate after 125 h, caused by the reduced concentration of water vapor in the atmosphere due to the lower water vapor partial pressure ($p_{\text{H}_2\text{O}}$). For the Si:Yb(2:1) coated Si_3N_4 substrate an initial mass loss caused by corrosion was followed by the increasing rate of oxidation reactions after 25 h, which led to a gradual gain in mass up to 125 h. However, in the following period up to 200 h, a lower mass loss was detected despite the reduction of the $p_{\text{H}_2\text{O}}$ to 0.08 atm, which will be explained in detail below.

In wet environments, the oxidation rate of Si_3N_4 is up to 20 times higher than in dry O_2 , which follows the mechanism of Equation (3) and is enhanced by the oxidation of the released NH_3 to H_2O (Equation (4)).^[15–17,55] Si_3N_4 usually forms a protective and efficient silica layer at high temperatures in air, however at temperatures above 1200 °C, the volatilization of $\text{Si}(\text{OH})_4$ leads to a significant mass loss and surface recession of the Si_3N_4 ceramic due to active corrosion (Equation (5)).^[11,16,17,19] Moreover, other effects such as the faster crystallization of SiO_2 , the diffusion of sintering additives and impurities from the bulk of Si_3N_4 , their precipitation as silicates and the reduction of the viscosity of the forming SiO_2 layer were reported for wet environments, increasing oxidation and corrosion rates.^[17,18,20,72,90–94]

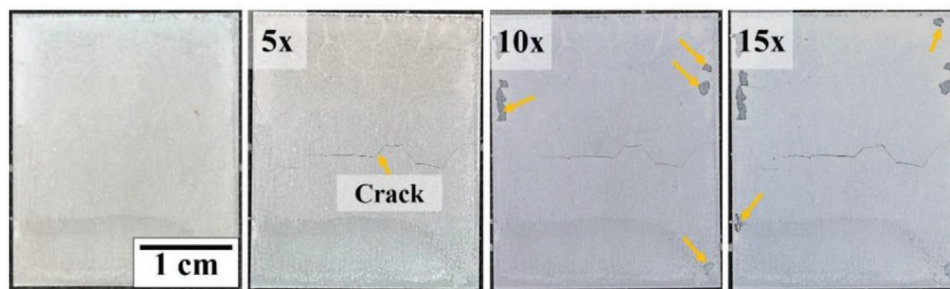


Figure 11. Photos of the surface of the Si:Yb(2:1) coating system on Si_3N_4 after several thermal shock cycles between 1200 and 20 °C.

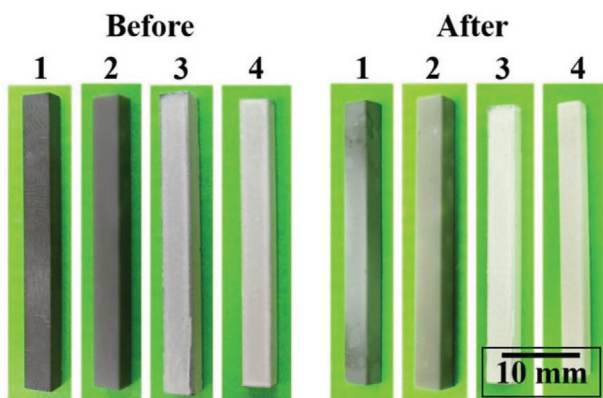


Figure 12. Photos of the uncoated Si_3N_4 substrates (1 and 2) and Si:Yb(2:1) coated Si_3N_4 (3 and 4) before and after the hot gas corrosion test at $1200\text{ }^\circ\text{C}$ for 200 h ($\nu = 100\text{ m s}^{-1}$).

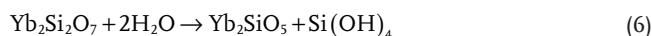


After the exposure for 200 h at $1200\text{ }^\circ\text{C}$ during the hot gas corrosion test, XRD analysis of the uncoated Si_3N_4 substrate detected the crystallization of SiO_2 as α -cristobalite together with the main crystalline peaks of $\text{Y}_2\text{Si}_2\text{O}_7$ and MgSiO_3 (Figure 13b). SEM/EDS analysis of the surface of the Si_3N_4 substrate confirmed the formation of pure SiO_2 , in addition to Y and Mg containing SiO_2 , referred to as Y- and Mg- SiO_2 (Figure 14a). However, no clear distinction of $\text{Y}_2\text{Si}_2\text{O}_7$ and MgSiO_3 was possible by SEM/EDS analysis due to the scarce detection of Y and Mg. In both Y and Mg containing SiO_2 phases the additional detection of Ca and Al resembled the composition of the glassy SiO_2 phase at the grain boundaries of $\text{Yb}_2\text{Si}_2\text{O}_7$ (refer to Figure 8). Based on these results, a composition of $\text{Ca}_{0.03}\text{Al}_{0.05}\text{Y}_{0.03}\text{SiO}$ can be estimated for Y- SiO_2 and $\text{Ca}_{0.9}\text{Al}_{0.04}\text{Mg}_{0.07}\text{SiO}_{2.7}$ for the Mg- SiO_2 . Despite the fast

corrosion of SiO_2 at $1200\text{ }^\circ\text{C}$ by water vapor, a $2.5\text{ }\mu\text{m}$ thick SiO_2 layer was still present in the cross-section of the corroded Si_3N_4 substrate (Figure 14b), which could be a consequence of the lower $p_{\text{H}_2\text{O}}$ during the last 75 h of the test, responsible for lower corrosion rates.

SEM/EDS analysis of the surface of the coated Si_3N_4 after hot gas corrosion showed the elimination of the glassy SiO_2 phase from the coating system (Figure 7a). This explains the mass loss during the first 25 h, also increasing the amount of open porosity to 11 vol% estimated by image analysis, which is higher than measured for the Yb(2:1) top-coat after pyrolysis (4 vol%, Figure 8).

The detailed analysis of the $\text{Yb}_2\text{Si}_2\text{O}_7$ grains revealed the formation of nanopores (Figure 15b), which should result from the corrosion of $\text{Yb}_2\text{Si}_2\text{O}_7$, thus yielding Yb_2SiO_5 , Yb_2O_3 , and volatile silanols through the corrosion mechanisms of Equations (6) and (7).^[19,25,29,31] However, neither Yb_2SiO_5 nor Yb_2O_3 were detected by means of XRD (Figure 13b) or SEM/EDS.



The preferred corrosion of the SiO_2 phases in deeper coating regions was also observed by the analysis of the cross-section of the Si:Yb(2:1) coating system, showing the formation of pores up to the interface with the Si_3N_4 substrate (Figure 15c). Hence, only residual SiO_2 was later detected by SEM/EDS analysis between the $\text{Yb}_2\text{Si}_2\text{O}_7$ grains as indicated in Figure 15d. The exposure for 200 h at $1200\text{ }^\circ\text{C}$ also led to the formation of some additional cracks in the bond-coat, possibly resulting from the crystallization of SiO_2 (Figure 15e).^[27]

Whereas the mass loss up to 25 h resulted from the corrosion of SiO_2 at the surface of the Si:Yb(2:1) coating system, the corrosion between 25 and 125 h was presumably controlled by the slower inward permeation of moisture into the pores of the coating and the formation of volatile $\text{Si}(\text{OH})_4$ from the SiO_2

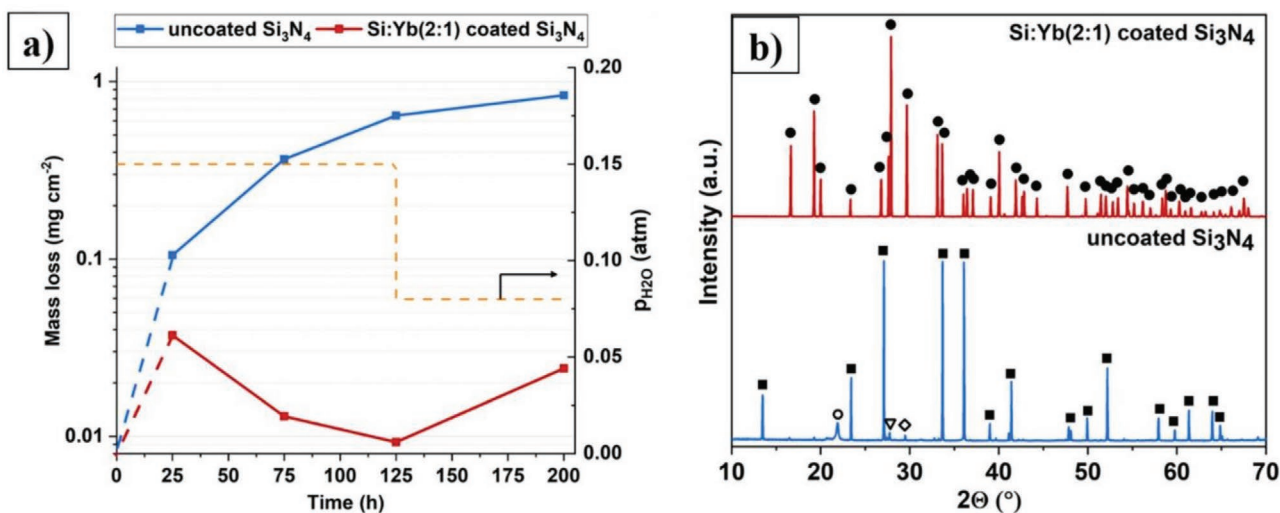


Figure 13. a) Mass loss over time and b) XRD analysis of the tested samples after the hot gas corrosion test at $1200\text{ }^\circ\text{C}$ for 200 h ($\nu = 100\text{ m s}^{-1}$) (■ – β - Si_3N_4 (00-033-1160); ● – α -cristobalite (00-039-1425); ▽ – $\text{Y}_2\text{Si}_2\text{O}_7$ (00-022-1103); ◇ – MgSiO_3 (04-020-1659); ● – β - $\text{Yb}_2\text{Si}_2\text{O}_7$ (00-025-1345)).

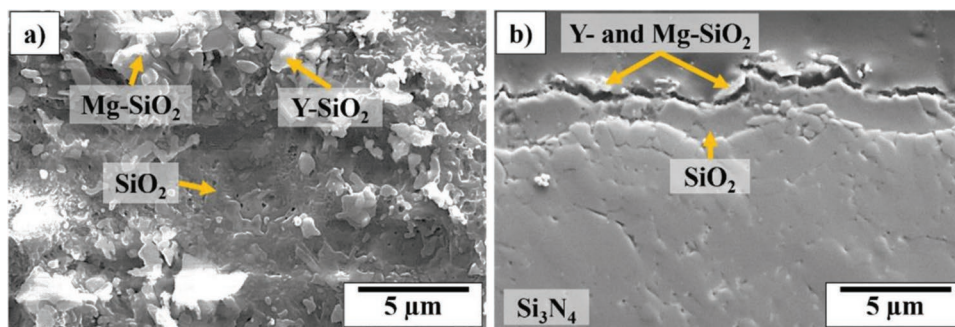


Figure 14. SEM micrographs of the a) surface and b) cross-section of uncoated Si_3N_4 after the hot gas corrosion test at $1200\text{ }^\circ\text{C}$ for 200 h.

phases.^[11] This mass loss was overcompensated by the oxidation of residual elemental Si in the bond-coat, which led to a gain in mass within this time interval. This consideration is supported by the fact that the bond-coat expanded from a thickness of 10 to 20 μm , following the mechanisms of Equations (8) and (9) (compare Figure 15c and Figure 9a). The low mass loss within the last 75 h mainly resulted from the corrosion of SiO_2 from the bond-coat as the silica in the grain boundaries of $\text{Yb}_2\text{Si}_2\text{O}_7$ already volatilized (see Figure 13a and Figure 15c).



As one of the most important results of the presented study, the corrosion rate of the coated samples was effectively reduced under these very harsh conditions. A further improvement in the long-term stability of the Si:Yb(2:1) coating system on Si_3N_4 is expected if the formation of the glassy SiO_2 phase between the $\text{Yb}_2\text{Si}_2\text{O}_7$ crystallites can be impeded.

4. Conclusion

In this study, we demonstrated that an easy-to-apply double-layered EBC system consisting of an in situ generated $\text{Yb}_2\text{Si}_2\text{O}_7$ top-layer and a Si-based bond-coat protects non-oxide ceramics like silicon nitride very effectively in extremely harsh conditions that prevail in stationary turbines and aircraft engines. In contrast to expensive conventional coating methods like physical vapor deposition and plasma spraying for the processing of thermal and environmental barrier coatings, the top layer composed of the oligosilazane Durazane 1800 and the active fillers Si and Yb_2O_3 as well as the bond coat composed of the silazane Durazane 2250 and Si-powder were applied via dipping and spraying onto a silicon nitride substrate. This approach enables the coating of even very complex shaped components.

Preliminary investigations on monoliths processed from Yb(2:1) top-coating composition confirmed the quantitative in situ formation and the pressureless sintering of $\beta\text{-Yb}_2\text{Si}_2\text{O}_7$ during pyrolysis at a temperature of $1415\text{ }^\circ\text{C}$ for 5 h in air. Because of 4.5 vol% residual open porosity the application

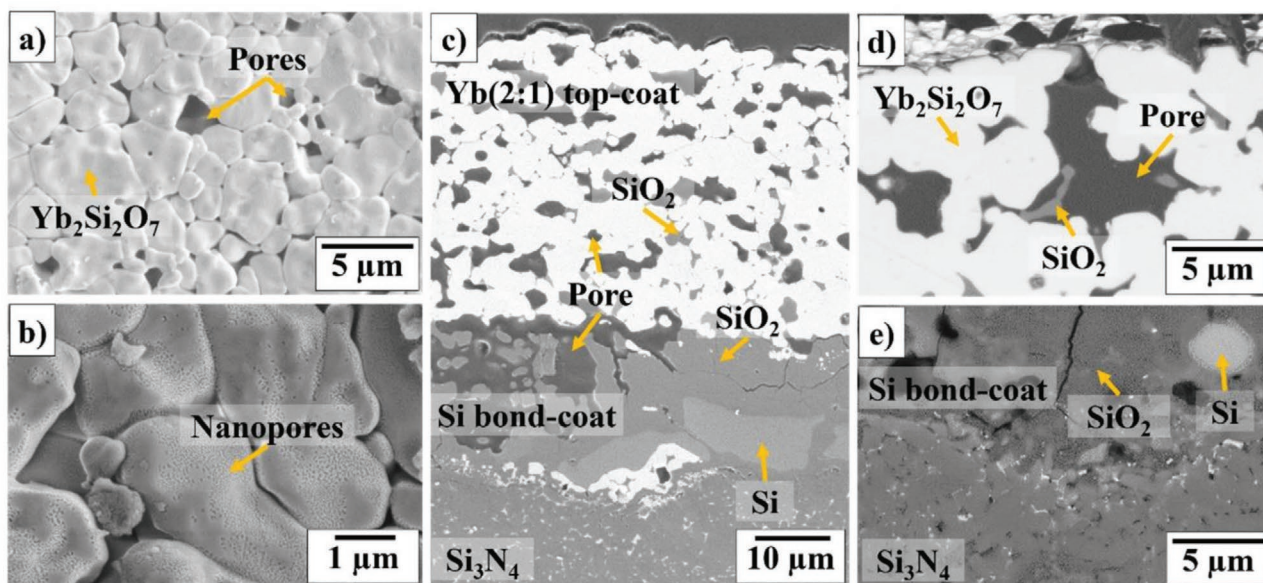


Figure 15. SEM micrographs of the a,b) surface and c–e) cross-section of the Si:Yb(2:1) coating system on Si_3N_4 after the hot gas corrosion test at $1200\text{ }^\circ\text{C}$ for 200 h.

of a bond-coat was necessary to protect the Si₃N₄ substrate against oxidation during pyrolysis and densification of the Yb(2:1) top-coat (1415 °C, 5 h, air). The resulting double-layer coating system Si:Yb(2:1) exhibited a dense microstructure with a total thickness of 68 μm, excellent adhesion strength (36.9 ± 6.2 MPa), hardness (6.9 ± 1.6 GPa), and scratch resistance (28 N). The remarkable protection potential was confirmed after 15 thermal cycles between 1200 and 20 °C by quenching in water with only minor signs of spallation. Finally, the hot gas corrosion behavior of the coated Si₃N₄ substrates was evaluated by very harsh tests carried out at 1200 °C for 200 h ($p = 1$ atm, $p_{\text{H}_2\text{O}} = 0.15$ atm, and $v = 100$ m s⁻¹). The developed coating system effectively reduced the mass loss caused by hot gas corrosion by 96% after 200 h when compared to the uncoated Si₃N₄ substrates. The excellent thermomechanical properties and the corrosion resistance of the in situ generated Yb₂Si₂O₇ coating system in extreme combustion environments confirms its high potential for protecting non-oxide Si₃N₄, SiC, and SiC/SiC ceramics in the next generation of gas turbines.

Acknowledgements

The authors would like to thank DFG (Deutsche Forschungsgemeinschaft) for the financial support within the projects 453000562 (MO 851/20) and by the Federal Ministry of Germany for Economic Affairs and Energy (BMWi) in the frame of the ZIM cooperation program project number ZF4109902AG7. The authors also acknowledge Hagen Klemm from Fraunhofer-IKTS for the fruitful discussion about the results regarding the hot gas corrosion test.

Open access funding enabled and organized by Projekt DEAL.

Conflict of Interest

The authors declare no conflict of interest.

Data Availability Statement

The data that support the findings of this study are available from the corresponding author upon reasonable request.

Keywords

environmental barrier coating, hot gas corrosion, polymer derived ceramic, rare-earth silicates, silazanes, silicon nitride

Received: November 17, 2021

Revised: January 19, 2022

Published online: February 11, 2022

- [1] CO₂ Emissions from Fuel Combustion 2020, <https://www.iea.org/reports/co2-emissions-from-fuel-combustion-overview> (accessed: February 2021).
- [2] Energy Technology Perspectives 2012, <https://www.iea.org/reports/energy-technology-perspectives-2012> (accessed: February 2021).
- [3] Global Energy & CO₂ Status Report 2019, <https://www.iea.org/reports/global-energy-co2-status-report-2019> (accessed: February 2021).

- [4] B. McLellan, N. Florin, D. Giurco, Y. Kishita, K. Itaoka, T. Tezuka, *Proc. CIRP* **2015**, 29, 138.
- [5] H. Kobayashi, A. Hayakawa, K. D. K. A. Somaratne, E. C. Okafor, *Proc. Combust. Inst.* **2019**, 37, 109.
- [6] M. P. Boyce, *Gas Turbine Engineering Handbook*, Elsevier Inc., Amsterdam **2012**.
- [7] T. M. Pollock, S. Tin, *J. Propul. Power* **2006**, 22, 361.
- [8] S. Cruchley, H. Evans, M. Taylor, *Mater. High Temp.* **2016**, 33, 465.
- [9] A. G. Evans, J. W. Hutchinson, *Surf. Coat. Technol.* **2007**, 201, 7905.
- [10] B. T. Richards, H. N. G. Wadley, *J. Eur. Ceram. Soc.* **2014**, 34, 3069.
- [11] E. J. Opila, N. S. Jacobson, D. L. Myers, E. H. Copland, *JOM* **2006**, 58, 22.
- [12] G. H. Meier, F. S. Pettit, K. Onal, *Report*, University of Pittsburg **2002**.
- [13] A. Sato, Y.-L. Chiu, R. C. Reed, *Acta Mater.* **2011**, 59, 225.
- [14] H. T. Lin, M. K. Ferber, *J. Eur. Ceram. Soc.* **2002**, 22, 2789.
- [15] N. S. Jacobson, *J. Am. Ceram. Soc.* **1993**, 76, 3.
- [16] D. S. Fox, E. J. Opila, Q. G. N. Nguyen, D. L. Humphrey, S. M. Lewton, *J. Am. Ceram. Soc.* **2003**, 86, 1256.
- [17] E. J. Opila, R. C. Robinson, D. S. Fox, R. A. Wenglarz, M. K. Ferber, *J. Am. Ceram. Soc.* **2003**, 86, 1262.
- [18] E. J. Opila, N. S. Jacobson, in *Materials Science Technology* (Eds: R. W. Cahn, P. Haasen, E. J. Kramer), Wiley-VCH, Weinheim, Germany **2013**, Ch. Corrosion of Ceramic Materials.
- [19] H. Klemm, *J. Am. Ceram. Soc.* **2010**, 93, 1501.
- [20] H. Klemm, *J. Eur. Ceram. Soc.* **2002**, 22, 2735.
- [21] F. Zok, *Am. Ceram. Soc. Bull.* **2016**, 95, 22.
- [22] K. N. Lee, D. S. Fox, N. P. Bansal, *J. Eur. Ceram. Soc.* **2005**, 25, 1705.
- [23] M. Fritsch, H. Klemm, M. Herrmann, B. Schenk, *J. Eur. Ceram. Soc.* **2006**, 26, 3557.
- [24] S. Ueno, D. D. Jayaseelan, T. Ohji, H. T. Lin, *J. Ceram. Process Res.* **2005**, 6, 81.
- [25] S. Ueno, D. D. Jayaseelan, H. Kita, T. Ohji, H. T. Lin, *Key Eng. Mater.* **2006**, 317–318, 557.
- [26] T. Bhatia, V. Vedula, H. Eaton, E. Sun, J. Holowczak, G. Linsey, in *Proc. ASME Turbo Expo 2004*, American Society Of Mechanical Engineers, Vienna, Austria **2004**, 431–438.
- [27] B. T. Richards, K. A. Young, F. De Francqueville, S. Sehr, M. R. Begley, H. N. G. Wadley, *Acta Mater.* **2016**, 106, 1.
- [28] Y. Wang, J. Liu, *J. Eur. Ceram. Soc.* **2009**, 29, 2163.
- [29] N. Maier, K. G. Nickel, G. Rixecker, *J. Eur. Ceram. Soc.* **2007**, 27, 2705.
- [30] G. Bocquillon, C. Chateau, C. Loriers, J. Loriers, *J. Solid State Chem.* **1977**, 20, 135.
- [31] M. Ridley, E. Opila, *J. Eur. Ceram. Soc.* **2020**, 41, 3141.
- [32] M. Wada, T. Matsudaira, N. Kawashima, S. Kitaoka, M. Takata, *Acta Mater.* **2017**, 135, 372.
- [33] T. Matsudaira, M. Wada, N. Kawashima, M. Takeuchi, D. Yokoe, T. Kato, M. Takata, S. Kitaoka, *J. Eur. Ceram. Soc.* **2020**, 41, 3150.
- [34] E. Bakan, D. Marcano, D. Zhou, Y. J. Sohn, G. Mauer, R. Vaßen, *J. Therm. Spray Technol.* **2017**, 26, 1011.
- [35] K. N. Lee, *J. Am. Ceram. Soc.* **2019**, 102, 1507.
- [36] T. Bhatia, G. V. Srinivasan, S. V. Tulyani, R. A. Barth, V. R. Vedula, W. K. Tredway, in *Proc. ASME Turbo Expo*, American Society Of Mechanical Engineers, Montreal, Canada **2007**, p. 281–288.
- [37] N. P. Padture, *npj Mater. Degrad.* **2019**, 3, 11.
- [38] E. Bakan, Y. J. Sohn, W. Kunz, H. Klemm, R. Vaßen, *J. Eur. Ceram. Soc.* **2019**, 39, 1507.
- [39] S. N. Basu, T. Kulkarni, H. Z. Wang, V. K. Sarin, *J. Eur. Ceram. Soc.* **2008**, 28, 437.
- [40] J. Xu, V. K. Sarin, S. Dixit, S. N. Basu, *Int. J. Refract. Met. Hard Mater.* **2015**, 49, 339.
- [41] P. Colombo, G. Mera, R. Riedel, G. D. Sorarù, *J. Am. Ceram. Soc.* **2010**, 93, 1805.

- [42] G. Barroso, Q. Li, R. K. Bordia, G. Motz, *J. Mater. Chem. A* **2019**, *7*, 1936.
- [43] S. Attia, J. Wang, G. Wu, J. Shen, J. Ma, *J. Mater. Sci. Technol.* **2002**, *18*, 211.
- [44] S. Ueno, D. D. Jayaseelan, N. Kondo, T. Ohji, S. Kanzaki, H. T. Lin, *Key Eng. Mater.* **2005**, *287*, 449.
- [45] D. D. Jayaseelan, S. Ueno, T. Ohji, S. Kanzaki, *Mater. Chem. Phys.* **2004**, *84*, 192.
- [46] G. Motz, T. Schmalz, S. Trassl, R. Kempe, in *Design, Processing and Properties of Ceramic Materials from Pre-ceramic Precursors* (Ed: S. Bernard), Nova Science Publishers Inc., New York, USA **2011**, pp. 15–36.
- [47] P. Greil, *J. Am. Ceram. Soc.* **1995**, *78*, 835.
- [48] M. Günthner, K. Wang, R. K. Bordia, G. Motz, *J. Eur. Ceram. Soc.* **2012**, *32*, 1883.
- [49] M. Günthner, T. Kraus, A. Dierdorf, D. Decker, W. Krenkel, G. Motz, *J. Eur. Ceram. Soc.* **2009**, *29*, 2061.
- [50] M. Günthner, T. Kraus, W. Krenkel, G. Motz, A. Dierdorf, D. Decker, *Int. J. Appl. Ceram. Technol.* **2009**, *6*, 373.
- [51] M. Günthner, A. Schütz, U. Glatzel, K. Wang, R. K. Bordia, O. Greißl, W. Krenkel, G. Motz, *J. Eur. Ceram. Soc.* **2011**, *31*, 3003.
- [52] K. Wang, M. Günthner, G. Motz, R. K. Bordia, *J. Eur. Ceram. Soc.* **2011**, *31*, 3011.
- [53] M. L. Leite, G. Barroso, M. Parchovianský, D. Galusek, E. Ionescu, W. Krenkel, G. Motz, *J. Eur. Ceram. Soc.* **2017**, *37*, 5177.
- [54] H. F. Chen, H. Klemm, *Adv. Eng. Ceram. Compos.* **2011**, 139.
- [55] B. E. Deal, A. S. Grove, *J. Appl. Phys.* **1965**, *36*, 3770.
- [56] K. H. Stern, *Report*, Naval Research Laboratory **1986**.
- [57] N. F. Mott, S. Rigo, F. Rochet, A. M. Stoneham, *Philos. Mag. B* **1989**, *60*, 189.
- [58] M. Németh-Sallay, Barna, L., I. C. Szép, *Phys. Status Solidi* **1977**, *43*, K135.
- [59] N. F. Mott, *Philos. Mag. B* **1987**, *55*, 117.
- [60] T. L. Christiansen, O. Hansen, J. A. Jensen, E. V. Thomsen, *ECS J. Solid State Sci. Technol.* **2014**, *3*, N63.
- [61] A. G. Revesz, B. J. Mrstik, H. L. Hughes, in *The Physics and Technology of Amorphous SiO₂* (Ed: R. A. B. Devine), Springer, Boston MA, USA **1988**, p. 297.
- [62] G. Ziegler, H. J. Kleebe, G. Motz, H. Müller, S. Traßl, W. Weibelzahl, *Mater. Chem. Phys.* **1999**, *61*, 55.
- [63] O. Flores, T. Schmalz, W. Krenkel, L. Heymann, G. Motz, *J. Mater. Chem. A* **2013**, *1*, 15406.
- [64] T. Miyazaki, S. Usami, R. Inoue, Y. Kogo, Y. Arai, *Ceram. Int.* **2019**, *45*, 9560.
- [65] E. Garcia, H. Lee, S. Sampath, *J. Eur. Ceram. Soc.* **2019**, *39*, 1477.
- [66] B. T. Richards, H. Zhao, H. N. G. Wadley, *J. Mater. Sci.* **2015**, *50*, 7939.
- [67] Y.-C. Zhou, C. Zhao, F. Wang, Y.-J. Sun, L.-Y. Zheng, X.-H. Wang, *J. Am. Ceram. Soc.* **2013**, *96*, 3891.
- [68] H. Salmang, H. Scholze, *Keramik*, Springer, Berlin, Germany **2007**.
- [69] S.-B. Wang, Y.-R. Lu, Y.-X. Chen, *Int. J. Appl. Ceram. Technol.* **2015**, *12*, 1140.
- [70] M. K. Cinibulk, *Ph.D. Thesis*, University of California **1991**.
- [71] F. Riley, *Progress in Nitrogen Ceramics*, Springer, Dordrecht, Netherlands **1983**.
- [72] Y. G. Gogotsi, V. A. Lavrenko, *Corrosion of High-Performance Ceramics*, Springer, Berlin, Germany **1992**.
- [73] H.-J. Choi, J.-G. Lee, Y.-W. Kim, *J. Mater. Sci.* **1997**, *32*, 1937.
- [74] H. Klemm, C. Taut, G. Wötting, *J. Eur. Ceram. Soc.* **2003**, *23*, 619.
- [75] F. Monteverde, A. Bellosi, *J. Eur. Ceram. Soc.* **1998**, *18*, 2313.
- [76] G.-H. Zhang, K.-C. Chou, K. Mills, *ISIJ Int.* **2012**, *52*, 355.
- [77] M. Futakawa, R. W. Steinbrech, *J. Am. Ceram. Soc.* **1998**, *81*, 1819.
- [78] V. Pareek, D. A. Shores, *J. Am. Ceram. Soc.* **1991**, *74*, 556.
- [79] G. Zhang, Y. Xu, D. Xu, D. Wang, Y. Xue, W. Su, *High Press. Res.* **2008**, *28*, 641.
- [80] S. Zhang, S. Tie, F. Zhang, *Micro Nano Lett.* **2018**, *13*, 1465.
- [81] P. Bettermann, F. Liebau, *Contrib. Mineral. Petrol.* **1975**, *53*, 25.
- [82] D. H. Olson, J. T. Gaskins, J. A. Tomko, E. J. Opila, R. A. Golden, G. J. K. Harrington, A. L. Chamberlain, P. E. Hopkins, *Scr. Mater.* **2020**, *177*, 214.
- [83] D. Chen, A. Pegler, M. Dorfman, *J. Am. Ceram. Soc.* **2020**, *103*, 4840.
- [84] A. Lee, J. W. Elam, S. B. Darling, *Environ. Sci.: Water Res. Technol.* **2016**, *2*, 17.
- [85] H. Yang, Y. Yang, X. Cao, X. Huang, Y. Li, *Ceram. Int.* **2020**, *46*, 27292.
- [86] S. J. Bull, E. G. Berasetegui, *Tribol. Int.* **2006**, *39*, 99.
- [87] P. J. Burnett, D. S. Rickerby, *Thin Solid Films* **1987**, *154*, 403.
- [88] D. P. H. Hasselman, *J. Am. Ceram. Soc.* **1967**, *50*, 454.
- [89] D. P. H. Hasselman, *J. Am. Ceram. Soc.* **1969**, *52*, 600.
- [90] T. Sato, K. Haryu, T. Endo, M. Shimada, *J. Mater. Sci.* **1987**, *22*, 2635.
- [91] M. Yoshimura, J. Kase, S. Sōmiya, in *Hydrothermal Reactions for Materials Science and Engineering* (Ed: S. Sōmiya), Springer, Dordrecht, Netherlands **1989**, p. 450.
- [92] M. Yoshimura, J. Kase, S. Sōmiya, *J. Mater. Res.* **1986**, *1*, 100.
- [93] P. F. Tortorelli, K. L. More, *J. Am. Ceram. Soc.* **2003**, *86*, 1249.
- [94] T. Cheng, P. F. Tortorelli, *J. Am. Ceram. Soc.* **2013**, *96*, 2330.
- [95] A. Morlier, S. Cros, J.-P. Garandet, N. Alberola, *Thin Solid Films* **2012**, *524*, 62.
- [96] C. A. Schneider, W. S. Rasband, K. W. Eliceiri, *Nat. Methods* **2012**, *9*, 671.